Analysis of Winding slot and Stator-Rotor Pole Combinations of Modular Transverse Flux-Switching Permanent Magnet Machine

Lujia Xie¹, Tianli Liu², Yongjian Li², Peng Su², and Guishu Zhao³*

¹School of Electronic Information and Automation, Civil Aviation University of China, Tianjin 300300, China
²State Key Laboratory of Intelligent Power Distribution Equipment and System, Hebei University of Technology, Tianjin 300401, China
³School of Electrical and Automation Engineering, Nanjing Normal University, Nanjing 210023, China

(Received 18 February 2025, Received in final form 26 June 2025, Accepted 30 June 2025)

This paper investigates the influence of winding slot and stator/rotor pole combinations on the electromagnetic torques of modular transverse flux-switching permanent magnet (MTFSPM) machine. Firstly, a unique winding factor calculation method for MTFSPM machines is proposed. By introducing the concept of virtual slots, the distribution factor of small virtual coils within a practical large coil and the distribution factor of the large coils are computed, which subsequently yields the overall winding factor of the MTFSPM machine. Additionally, based on the magnetic circuit method, the PM magnetomotive force (PM-MMF) amplitudes in slotted and unslotted regions are calculated, thus accounting for the influence of slot openings. Subsequently, based on different MMF permeance and winding function models, the back-electromotive force (back-EMF) amplitudes variation trends are calculated, leading to the identification of winding slot and stator/rotor pole combinations that offer higher output torque capability. Finally, the electromagnetic characteristics of candidate MTFSPM machines are compared through three-dimensional finite-element analysis, and experiments are conducted to verify the theoretical analysis.

Keywords: Winding factor, Permanent magnet magnetomotive force (PM-MMF), Winding function, Winding slot and stator-rotor pole combinations

1. Introduction

The flux-switching permanent magnet (FSPM) machine is considered a promising candidate for applications in electric vehicles, aerospace, and wind power generation due to its robust rotor structure, excellent thermal management capability, and high torque density [1-4]. However, the FSPM machine suffers from significant torque ripple caused by the flux-focusing effect and double salient structure [5]. Additionally, the further improvement of torque density is limited because both the PMs and armature windings are located on the stator [6].

Extensive research has been conducted on the suppression of cogging torque. Ref. [7] presents a switched reluctance machine with five sets of stator/rotor configurations distributed along the axial direction, which effectively reduces the machine's torque ripple. Ref. [8]

proposes a FSPM machine with dual-stator structure, which effectively reduced even-order harmonics. Ref. [9] introduces an axial-modular FSPM machine, which can effectively suppress cogging torque and thus reduce torque ripple through module combination technique. In addition, to improve the machine's output torque, a transverse flux (TF) machine is proposed [10]. The main magnetic flux path in this machine is transverse to the rotor's rotation direction, resulting in decoupling of electrical and magnetic loads [11, 12]. Therefore, TF machines are easily designed with a multi-pole structure and possess higher torque density [13]. Moreover, TF machines are primarily used in low-speed and high-torque applications [14]. Therefore, combining FSPM machines, axial modular topologies, and TF machines, this paper proposes a novel modular transverse FSPM (MTFSPM) machine, which features higher output torque and lower torque ripple.

In the design of machines, the combination of the winding slot number (N_s) , stator pole number (P_s) , and rotor pole number (P_r) plays a crucial role in determining

©The Korean Magnetics Society. All rights reserved.

*Corresponding author: e-mail: gzhao@njnu.edu.cn

the electromagnetic performance of the machine [15]. Ref. [16] compares the stator-rotor pole number combinations in FSPM machines from the perspectives of back electromotive force (EMF) and electromagnetic torque using analytical methods. The conclusion drawn is that the rotor pole number should be close to the stator pole number, and machines with a relatively higher rotor pole number tend to have larger output torque. Ref. [17] indicates that the air-gap surface occupation factor (ASOF) can assist in selecting the optimal stator-rotor pole combination and the number of winding phases for FSPM machines. Ref. [18], based on the flux harmonic theory, highlights the connection method of the windings and determines the required combinations of stator-rotor pole number to achieve symmetrical back-EMF waveforms. Reference [19] investigates the winding structure and the stator-rotor pole combinations principle of the doubly-fed FSPM machine based on the coil-back EMF vector diagrams. In reference [20], the effect of slot-pole combinations on the comprehensive performance of an ironless stator axial flux PM (AFPM) machine with nonoverlapping concentrated windings is investigated. The coil space utilization and winding factor for nonoverlapping concentrated windings are derived in formula form, and the output torque capability is compared. The copper mass and utilization rate under different slot numbers and stator diameters are analyzed. Reference [21] investigates the effect of different slot-pole combinations on machine losses and other performance parameters in a fractional-slot concentrated winding double-rotor Halbach array AFPM machine using Additive Manufacturing (AM) coils. Reference [22] examines the optimal slot-pole combinations for axial-field fluxmodulated machines by establishing flux linkage models and selecting combinations with low total harmonic distortion (THD). Additionally, slot-pole combinations with the highest winding factor and reasonable power factor are identified. Reference [23] selects slot-pole combinations with high output torque capabilities for multi-magnetic source AF modulation machines by considering winding factor, winding pole pair number, and pole ratio. However, the winding structure of the MTFSPM machine differs from that of traditional FSPM and AF machines, and the MTFSPM machine has a threedimensional modules combination configuration. Therefore, it is necessary to conduct research on the winding slot and stator-rotor pole combinations for the MTFSPM machine.

This paper aims to investigate the influence of $N_s/P_s/P_r$ combinations on the electromagnetic torque performances of MTFSPM machines, providing a basis for selecting

machines with high output torque capability. Section II investigates a unique winding factor calculation method for MTFSPM machines, resulting in machines with higher winding factors. Using the magnetic circuit method, this section also analyzes the impact of slotting on the PM magnetomotive force (MMF) amplitude, deriving the PM-MMF variation trend for different $N_s/P_s/$ P_r combinations. Additionally, fundamental back-EMF amplitudes are calculated using the MMF-permeance models and winding function models. These calculations allow for the selection of MTFSPM machines with high output torque potential under specific P_s values, namely: $6s/24p_s/13p_r$, $6s/18p_s/10p_r$, and $6s/12p_s/7p_r$ configurations. In Section III, the electromagnetic performances the three machines are compared based on three-dimensional finite-element analysis (3D-FEA). Then, the prototype machine is manufactured, and experimental verification is conducted in Section IV. Finally, conclusions are drawn in Section V.

2. Winding Slot and Stator-rotor Pole Combinations

2.1. Topology and winding factor

The topology of the MTFSPM machine is shown in Fig. 1. It consists of three modules: module α , module β , and module γ . The PMs of each module are magnetized tangentially, with adjacent PMs having opposite magnetization directions. Modules β and γ are identical. The axial length of module α is twice that of module β , with the magnetization direction of the PMs in module α and module β being the same, the winding directions being opposite, and the rotor teeth shifted by π/P_r in the circumferential direction, as shown in Fig. 2. The stator between different modules is connected by the stator core and PMs located in the stator yoke, while the rotor is connected by the rotor core. This special structure provides the machine with a transverse flux path, which alleviates the competition between magnetic load and

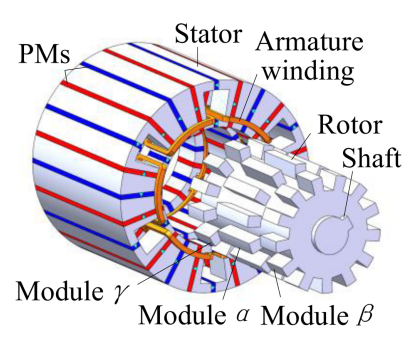


Fig. 1. (Color online) Topology of the MTFSPM machine.

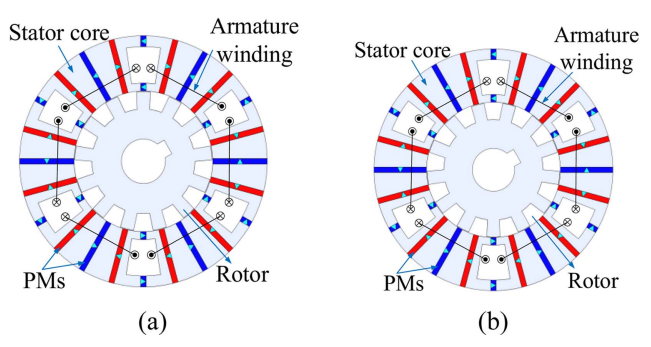


Fig. 2. (Color online) Cross sections of two modules of MTF-SPM machine. (a) Module α . (b) Module β .

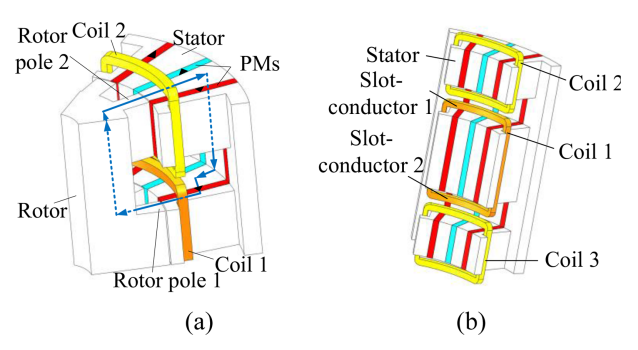


Fig. 3. (Color online) The $6s/24p_s/13p_r$ MTFSPM machine. (a) Transverse flux path. (b) Partial Schematic of the Stator.

electric load to some extent.

Due to the transverse flux path in the MTFSPM machine, as shown in Fig. 3(a), its winding factor calculation method differs from that of the traditional radial flux FSPM machine. In the MTFSPM machine, the effective slot conductors are distributed circumferentially rather than axially, as illustrated by slot conductors 1 and 2 in Fig. 3(b). Consequently, the pitch factor k_p of the MTFSPM machine is 1, and its winding factor k_w is determined solely by the distribution factor k_d .

The winding factor of the MTFSPM machine can be expressed as

$$k_{w} = k_{p}k_{d} = k_{p}k_{di}k_{do} \tag{1}$$

where k_{di} represents the distribution factor for the virtual small coils within a practical large coil, and k_{do} denotes the distribution factor between adjacent large coils. To calculate k_{di} , the concept of virtual slots is introduced, which assumes that a small slot is opened on each PM of the machine to accommodate small coils. For example, in the 6s/24ps/13pr MTFSPM machine, each large coil (e.g., coil A1) spans four stator teeth and can be equivalently represented by four small coils (e.g., coil a1, coil a2, coil a3, and coil a4), as shown in Fig. 4. The distribution factor k_{di} =0.958 for the small coils can be obtained from

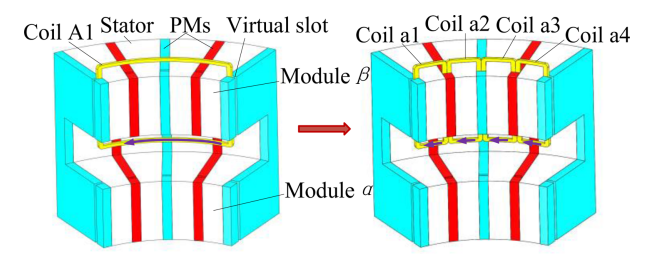


Fig. 4. (Color online) Equivalence of a large coil to four small coils via virtual slots.

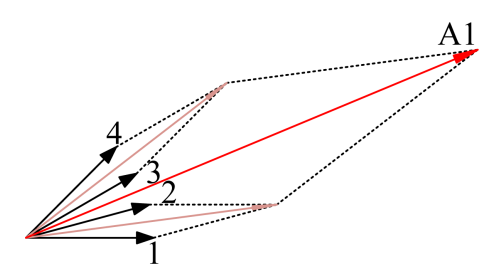


Fig. 5. (Color online) Slot-conductors back-EMF vectors distributions of the small coils of the 6s/24p_s/13p_r MTFSPM machine.

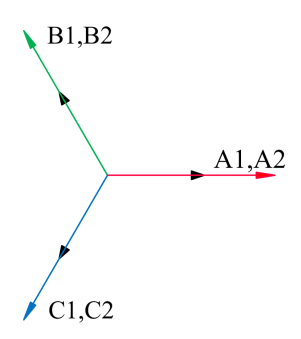


Fig. 6. (Color online) Slot-conductors back-EMF vectors distributions of the large coils of the 6s/24p_s/13p_r MTFSPM machine.

the slot conductors back-EMF vector distribution of the small coils, as shown in Fig. 5. Besides, the distribution factor k_{do} =1 between adjacent large coils, such as coils A1 and A2, can be derived from the back-EMF vector distribution of the large coils, as shown in Fig. 6. Thus, the winding factor of the $6s/24p_s/13p_r$ MTFSPM machine can be obtained as 0.958 using equation (1).

The PMs of the MTFSPM machine are alternately magnetized, and the designed machine is a three-phase machine. Furthermore, each coil of the winding can enclose several stator teeth and PMs, which distinguishes it from the traditional FSPM machine. Therefore, the number of stator poles in the MTFSPM machine does not necessarily equal the number of winding slots and can be expressed as:

$$P_{\rm s} = 6a \tag{2}$$

$$N_{s} = 3b \tag{3}$$

$$P_{s} = cN_{s} \tag{4}$$

The inherent advantage of MTFSPM machine lies in the capacity for each winding coil to span several stator teeth. This characteristic allows for a reduction in the number of winding slots, thereby alleviating the competition between magnetic and electric loads. Therefore, the case where a coil surrounds only one stator tooth is not considered, (i.e., $P_s \neq N_s$).

For the MTFSPM machine with a balanced three-phase winding, the winding slot number and the rotor pole number should satisfy the following relationship:

$$\frac{N_s}{GCD(N_s, P_a)} = 3i \tag{5}$$

where i is 1, 2, 3..., the armature winding pole pair number $P_a=N_s\pm P_r$, $GCD(N_s, P_a)$ denotes the greatest common divisor of N_s and P_a . Therefore, the feasible $N_s/P_s/P_r$ combinations for $P_s=24$, 18, and 12 are listed in Tables 1 to 8.

Based on the winding factor calculation results from Tables 1 to 8, the optimal combinations of $N_s/P_s/P_r$ for each considered configuration can be determined. However, unlike traditional FSPM machines, the MTFSPM machine removes a portion of the PMs at the slotting areas, which affects the machine's output torque. Specifically, for a given P_s , variations in N_s influence the machine's output torque. Therefore, the winding factor alone is insufficient to make a definitive judgment

Table 1. Combinations of N_s =3, P_s =24 and P_r for MTFSPM machines.

$GCD(P_s, P_a)$				$N_s=3, P_s$	=24		
	P_r	1	2	4	5	7	8
GCD=1	k_w	0.109	0.112	0.125	0.136	0.178	0.217
GCD-1	P_r	10	11	13	14	16	17
	k_w	0.418	0.829	0.829	0.418	0.217	0.178

Table 2. Combinations of N_s =6, P_s =24 and P_r for MTFSPM machines.

$\overline{\mathrm{GCD}\left(P_s,P_a\right)}$)	N_s =6, P_s =24						
GCD=1	P_r	1	5	7	11	13	17	
GCD=1	k_w	0.126	0.158	0.205	0.958	0.958	0.205	
GCD=2	P_r	2	4	8	10	14	16	
GCD-2	k_w	0.224	0.25	0.433	0.837	0.837	0.433	

Table 3. Combinations of N_s =12, P_s =24 and P_r for MTFSPM machines.

$\overline{\mathrm{GCD}\left(P_{s},P_{a}\right)}$)		İ	$V_s=12, P$	_s =24		
GCD=1	P_r	1	5	7	11	13	17
GCD-1	k_w	0.131	0.609	0.793	0.991	0.991	0.793
GCD=2	P_r	2	10	14	22		
GCD=2	k_w	0.259	0.966	0.966	0.259		
GCD=4	P_r	4	8	16	20		
GCD=4	k_w	0.5	0.866	0.866	0.5		

Table 4. Combinations of N_s =3, P_s =18 and P_r for MTFSPM machines.

$\overline{\mathrm{GCD}\left(P_s,P_a\right)}$)	N_s =3, P_s =18					
	P_r	1	2	4	5	7	8
CCD-1	k_w	0.147	0.154	0.188	0.225	0.422	0.831
GCD=1	P_r	10	11	13	14	16	17
	k_w	0.831	0.422	0.225	0.188	0.154	0.147

Table 5. Combinations of N_s =6, P_s =18 and P_r for MTFSPM machines.

$GCD(P_s, P_a)$)			N_s =6, P_s	=18		
GCD=1	P_r	1	5	7	11	13	17
GCD=1	k_w	0.293	0.449	0.844	0.844	0.449	0.293
GCD=2	P_r	2	4	8	10	14	16
GCD-2	k_w	0.177	0.218	0.96	0.96	0.218	0.177

Table 6. Combinations of N_s =9, P_s =18 and P_r for MTFSPM machines.

$\overline{\mathrm{GCD}\left(P_{s},P_{a}\right)}$)	$N_s = 9, P_s = 18$							
	P_r	1	2	4	5	7	8		
CCD 1	k_w	0.174	0.342	0.643	0.766	0.94	0.985		
GCD=1	P_r	10	11	13	14	16	17		
	k_w	0.985	0.94	0.766	0.643	0.342	0.174		
CCD-2	P_r	3	6	12	15				
GCD=3	k_w	0.5	0.866	0.866	0.5				

Table 7. Combinations of N_s =3, P_s =12 and P_r for MTFSPM machines.

$GCD(P_s, P_a)$		$N_s = 3, P_s = 12$						
	P_r	1	2	4	5	7	8	
GCD=1	k_w	0.224	0.25	0.433	0.837	0.837	0.433	
GCD=1	P_r	10	11	13	14	16	17	
	k_w	0.25	0.224	0.224	0.25	0.433	0.837	

Table 8. Combinations of N_s =6, P_s =12 and P_r for MTFSPM machines.

$GCD(P_s, P_a)$)			N_s =6, P_s	=12		
GCD=1	P_r	1	5	7	11	13	17
GCD-1	k_w	0.259	0.966	0.966	0.259	0.259	0.966
GCD=2	P_r	2	4	8	10	14	16
GCD=2	k_w	0.5	0.866	0.866	0.5	0.5	0.866

regarding the machine's $N_s/P_s/P_r$ combinations.

The machine's output torque can be expressed as

$$T_e = \frac{45}{n\pi} E_m I_m \tag{6}$$

where n represents the rotational speed, E_m is the back-EMF amplitude, and I_m is the phase current amplitude. Under the rated speed of n=1500r/min, by analyzing E_m and I_m , the output torques of different machines can be compared, thereby allowing the selection of the optimal $N_s/P_s/P_r$ combinations.

2.2. Back-EMF analysis

The PM-MMF models of the MTFSPM machines with different N_s/P_s combinations are shown in Fig. 7, where θ_{s1} represents the half-arc length of the PM, θ_{s2} is the sum of the stator tooth width and the half-arc length of the PM, $\theta_{s3}=\theta_{s1}+2\theta_{s2}$, and $\theta_{s4}=2\theta_{s1}+\theta_{s2}$. $F_{1_3s/24Ps}$, $F_{1_6s/24Ps}$, $F_{1_3s/18Ps}$, $F_{1_6s/18Ps}$, and $F_{1_3s/12Ps}$ represent the PM-MMF amplitudes in the unslotted regions for the corresponding N_s/P_s combinations. $F_{2_3s/24Ps}$, $F_{2_6s/18Ps}$, $F_{2_12s/24Ps}$, $F_{2_3s/18Ps}$, $F_{2_6s/18Ps}$, $F_{2_9s/18Ps}$, $F_{2_3s/12Ps}$, and $F_{2_6s/12Ps}$ represent the PM-MMF amplitudes in the slotted regions for the corresponding N_s/P_s combinations. Therefore, the PM-MMF of the MTFSPM machine can be expressed as

$$F_{PM}(\theta) = \sum_{n=1}^{\infty} F_{PMn} \sin(q\theta)$$
 (7)

where F_{PMn} represents the Fourier series coefficients of the PM-MMF, as shown in Table 9. For the combinations $3s/24p_s$, $6s/24p_s$, $12s/24p_s$, $3s/18p_s$, $9s/18p_s$, $6s/12p_s$, and $3s/12p_s$, the parameter q is defined as $q=nN_s$, where n is 1, 2, 3.... For the $6s/18p_s$ combination, $q=[(2n-1)/2]N_s$.

The PM-MMF amplitude is a key factor in determining the back-EMF. The PM-MMF amplitudes in the MTFSPM machine can be calculated using the equivalent magnetic circuit method. Fig. 8 illustrates the local equivalent magnetic circuit model of the $6s/24p_s$ MTFSPM machine, where the permeability of the iron core is assumed to be infinite. The MMF of the PM F_{PM} , the PM permeance in

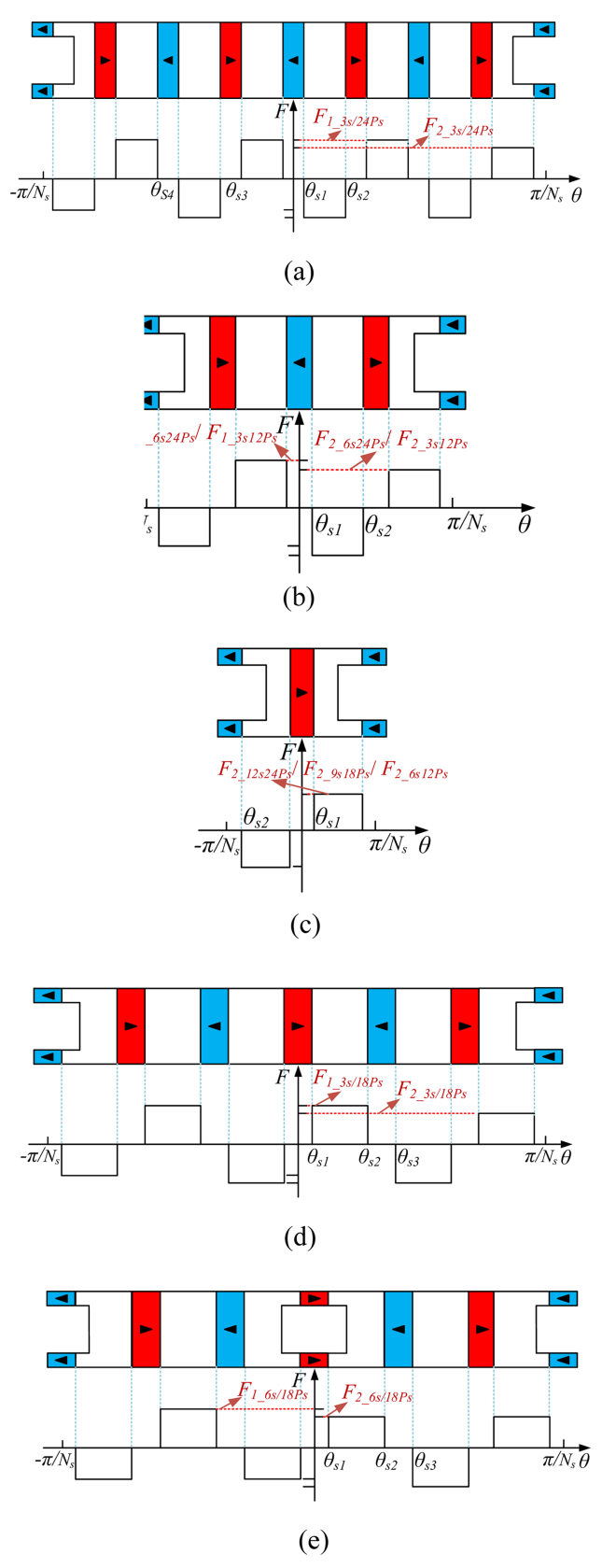


Fig. 7. (Color online) PM-MMF model. (a) $3s/24p_s$. (b) $6s/24p_s$, $3s/12p_s$. (c) $12s/24p_s$, $9s/18p_s$, $6s/12p_s$. (d) $3s/18p_s$. (e) $6s/18p_s$.

Table 9. PMM-MMF of the MTFSPM machines.

Cases	F_{PMn}
3s/24p _s	$\frac{2}{n\pi} \{ F_{1_{-3s/24Ps}} [\cos q\theta_{s2} - \cos q\theta_{s1} + \cos q\theta_{s3} - \cos q\theta_{s4} + \cos(n\pi - q\theta_{s3}) \\ -\cos(n\pi - q\theta_{s4})] + F_{1_{-3s/24Ps}} [\cos(n\pi - q\theta_{s2}) - \cos(n\pi - q\theta_{s1})] \}$
6s/24p _s	$\frac{2F_{1_{-}6s/24Ps}}{n\pi}(\cos q\theta_{s2} - \cos q\theta_{s1}) - \frac{2F_{2_{-}6s/24Ps}}{n\pi} \times [\cos(n\pi - q\theta_{s1}) - \cos(n\pi - q\theta_{s2})]$
12s/24p _s	$\frac{2F_{2_12s/24Ps}}{n\pi}(\cos q\theta_{s2}-\cos q\theta_{s1})$
3s/18p _s	$\frac{2}{n\pi} \{ F_{1_3s/18Ps} [\cos q\theta_{s1} - \cos q\theta_{s2} + \cos(n\pi - q\theta_{s3}) - \cos q\theta_{s3}] + F_{2_3s/18Ps} [\cos(n\pi - q\theta_{s2}) - \cos(n\pi - q\theta_{s1})] \}$
$6s/18p_s$	$\frac{4}{(2n-1)\pi} \left[F_{2_{-6s/18Ps}}(\cos q\theta_{s1} - \cos q\theta_{s2}) - F_{1_{-6s/18Ps}}\cos q\theta_{s3} \right]$
9s/18p _s	$\frac{2F_{2_9s/18Ps}}{n\pi}(\cos q\theta_{s2}-\cos q\theta_{s1})$
3s/12p _s	$\frac{2F_{1_{-}3s/12Ps}}{n\pi}(\cos q\theta_{s2} - \cos q\theta_{s1}) - \frac{2F_{2_{-}3s/12Ps}}{n\pi} \times [\cos(n\pi - q\theta_{s1}) - \cos(n\pi - q\theta_{s2})]$
6s/12p _s	$\frac{2F_{2_6s/12Ps}}{n\pi}(\cos q\theta_{s2}-\cos q\theta_{s1})$

the unslotted region Λ_{PMI} , the PM permeance in the slotted region Λ_{PM2} , and the air-gap permeance Λ_{gap} can be expressed as:

$$F_{PM} = H_c \omega_{PM} \tag{8}$$

$$\begin{cases}
\Lambda_{PM1} = \frac{l_{PM1}l_a\mu_0\mu_{PM}}{\omega_{PM}} \\
\Lambda_{PM2} = \frac{(l_{PM2} + l_{PM3})l_a\mu_0\mu_{PM}}{\omega_{PM}}
\end{cases}$$
(9)

$$\Lambda_{gap} = \frac{\mu_0 \omega_{st} l_a}{g} \tag{10}$$

where H_c represents the PM coercive, l_{PM1} is the length of the large PMs along the radial direction in the unslotted regions, while l_{pm2} and l_{pm3} are the lengths of the two smaller PMs along the radial direction in the slotted regions. w_{PM} and w_{st} denote the widths of the PMs and stator teeth, respectively, l_a is the axial length, and μ_0 and μ_r represent the air permeability and the relative permeability of the PMs, respectively.

Based on the equivalent magnetic circuit, the PM-MMF amplitudes $F_{1_6s/24Ps}$ and $F_{2_6s/24Ps}$ can be derived from equations (8) to (10).

$$\begin{bmatrix} \Lambda_{PM2}^{-1} + 2\Lambda_{gap}^{-1} & \Lambda_{gap}^{-1} & 0 & \cdots & 0 & \Lambda_{gap}^{-1} \\ \Lambda_{gap}^{-1} & \Lambda_{PM1}^{-1} + 2\Lambda_{gap}^{-1} & \Lambda_{gap}^{-1} & \cdots & 0 & 0 \\ \vdots & \vdots & \vdots & \ddots & \vdots & \vdots \\ \Lambda_{gap}^{-1} & 0 & 0 & \cdots & \Lambda_{gap}^{-1} & \Lambda_{PM1}^{-1} + 2\Lambda_{gap}^{-1} \end{bmatrix}$$

$$\begin{bmatrix} \Phi_{1} \\ \Phi_{2} \\ \vdots \\ \Phi_{24} \end{bmatrix} = \begin{bmatrix} F_{PM} \\ F_{PM} \\ \vdots \\ F_{PM} \end{bmatrix}$$

$$(11)$$

$$F_{1_6s/24Ps} = (\Phi_2 + \Phi_3)\Lambda_{gap}^{-1}$$
 (12)

$$F_{2_6s/24Ps} = (\Phi_1 + \Phi_2)\Lambda_{gap}^{-1}$$
 (13)

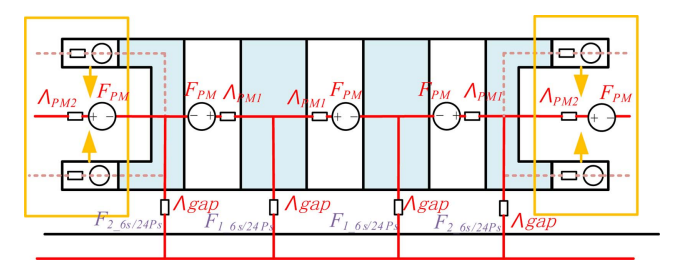


Fig. 8. (Color online) The equivalent magnetic circuit of the $6s/24p_s$ MTFSPM machine.

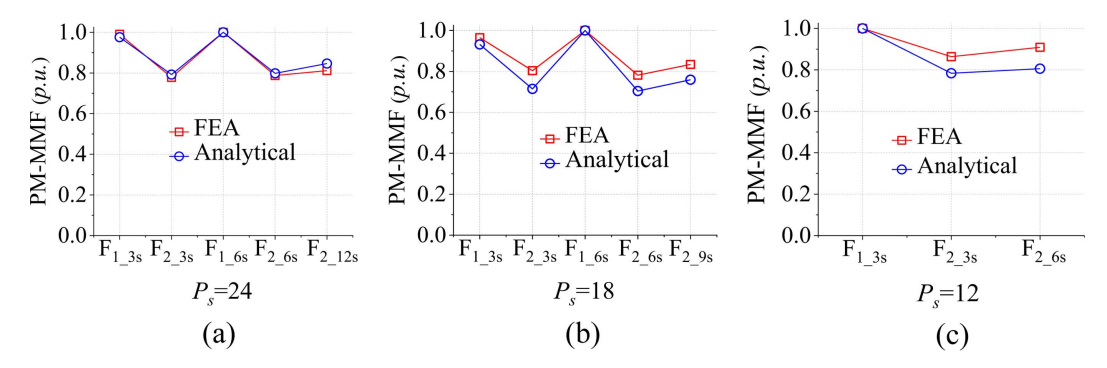


Fig. 9. (Color online) PM-MMF amplitudes with different N_s/P_s combinations of MTFSPM machines. (a) P_s =24. (b) P_s =18. (c) P_s =12.

where Φ_i (i[1,24]) represents the magnetic flux magnitude of the i-th loop.

Similarly, using the equivalent magnetic circuit method, the PM-MMF amplitudes for other N_s/P_s combinations of MTFSPM machines can be obtained. For a given value of P_s , the PM-MMF amplitudes of MTFSPM machines with different N_s are shown in Fig. 9. It can be observed that the trends of the analytical calculations are consistent with those of the FEA (3D-FEA). Additionally, it can be seen that the PM-MMF amplitudes F_1 at the slotted regions is lower than the PM-MMF amplitudes F_2 at the unslotted regions.

Fig. 10 shows the rotor permeance model of the MTFSPM machine, where θ_{rs} represents the rotor slot width and t_r denotes the rotor pole pitch. It can be observed that the angle between module α and module β (module γ) is π/P_r . Therefore, the rotor permeance of module α and module β (module γ) can be expressed as

$$\Lambda_{R\alpha}(\theta, t) = \Lambda_{R0} + \Lambda_{Rb} \sum_{k=1}^{\infty} \Lambda_{Rk} \cos[kP_r(\theta + \omega_r t + \theta_0)]$$
 (14)

$$\Lambda_{R\beta\gamma}(\theta,t) = \Lambda_{R0} + \Lambda_{Rb} \sum_{k=1}^{\infty} \Lambda_{Rk} \cos[kP_r(\theta + \omega_r t + \theta_0 + \frac{\pi}{P_r})]$$
 (15)

$$\Lambda_{R0} = \frac{1}{k_{...}} \tag{16}$$

$$\Lambda_{Rb}\Lambda_{Rk} = \frac{4}{k\pi} \left[0.5 + \frac{(k\varepsilon_r)^2}{0.78 - 2(k\varepsilon_r)^2}\right] \sin(1.6k\pi\varepsilon_r) \tag{17}$$

where

$$k_{cr} = \frac{t_r}{t_r - g \frac{\varepsilon_r^2}{5 + \varepsilon_r}}, \ \varepsilon_r = \frac{\theta_{rs}}{t_r}$$
 (18)

where g is the air-gap length.

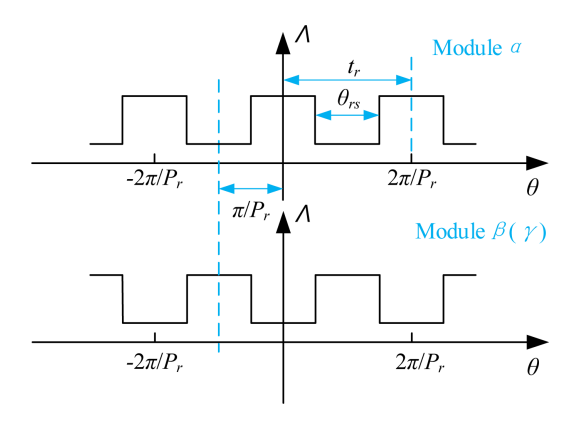


Fig. 10. (Color online) Air-gap permeance model of the MTF-SPM machine.

Based on the PM-MMF and rotor permeance, the PM flux density of the MTFSPM machine can be expressed as

$$B_{PM\alpha}(\theta,t) = \Lambda_{R0} \sum_{n=1}^{\infty} F_{PMn} \sin(q\theta) + \frac{\Lambda_{Rb}}{2} \sum_{n=1}^{\infty} \sum_{k=1}^{\infty} F_{PMn}$$

$$\Lambda_{Rk} \sin[(q \pm kP_r)\theta \pm kP_r(\omega_r t + \theta_0)]$$
(19)

$$B_{PM\beta\gamma}(\theta,t) = \Lambda_{R0} \sum_{n=1}^{\infty} F_{PMn} \sin(q\theta) + \frac{\Lambda_{Rb}}{2} \sum_{n=1}^{\infty} \sum_{k=1}^{\infty} F_{PMn}$$

$$\Lambda_{Rk} \sin[(q \pm kP_r)\theta \pm kP_r(\omega_r t + \theta_0 + \frac{\pi}{P})]$$
(20)

The winding function is another important factor that determines the back-EMF. The winding function models for the MTFSPM machine with different $N_s/P_s/P_r$ combinations are shown in Fig. 11, where $\theta_{s5}=3\theta_{s1}+2\theta_{s2}$, $\theta_{s6}=2\theta_{s1}+3\theta_{s2}$, $\theta_{s7}=4\theta_{s1}+3\theta_{s2}$, $\theta_{s8}=3\theta_{s1}+4\theta_{s2}$, $\theta_{s9}=5\theta_{s1}+4\theta_{s2}$, $\theta_{s10}=4\theta_{s1}+5\theta_{s2}$, $\theta_{s11}=6\theta_{s1}+5\theta_{s2}$, and $\theta_{s12}=5\theta_{s1}+6\theta_{s2}$. For the combinations $3s/24p_s/11p_r$ ($13p_r$), $3s/18p_s/8p_r$ ($10p_r$), $9s/18p_s/8p_r$ ($10p_r$), and $3s/12p_s/5p_r$ ($7p_r$), the winding function can be expressed as

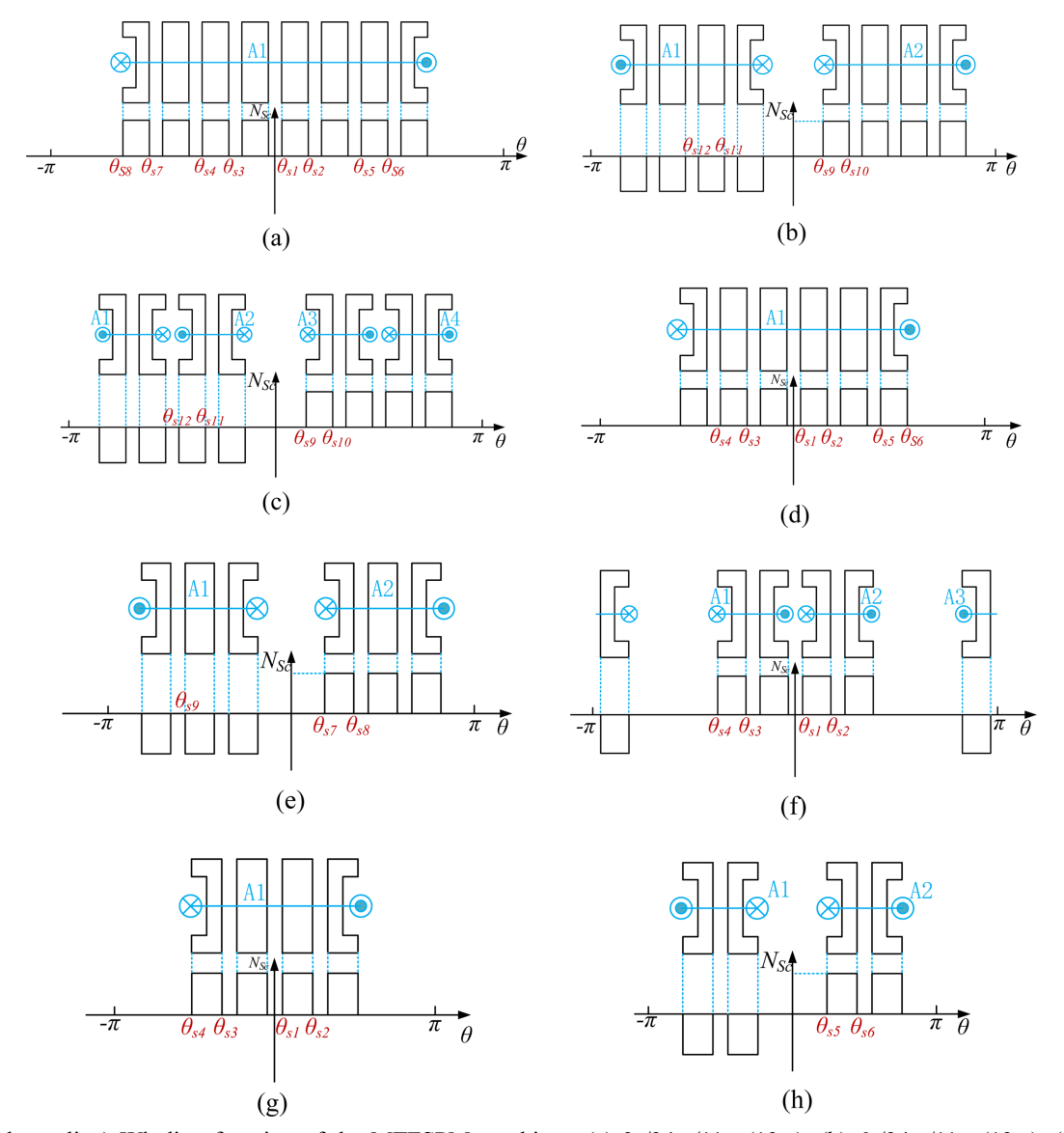


Fig. 11. (Color online) Winding function of the MTFSPM machines. (a) $3s/24p_s/11p_r$ ($13p_r$). (b) $6s/24p_s/11p_r$ ($13p_r$). (c) $12s/24p_s/11p_r$ ($13p_r$). (d) $3s/18p_s/8p_r$ ($10p_r$). (e) $6s/18p_s/8p_r$ ($10p_r$). (f) $9s/18p_s/8p_r$ ($10p_r$). (g) $3s/12p_s/5p_r$ ($7p_r$). (h) $6s/12p_s/5p_r$ ($7p_r$).

$$\begin{cases} N_{\alpha}(\theta) = N_{\alpha 0} + \sum_{i=1}^{\infty} N_{\alpha i} \cos i\theta \\ N_{\beta \gamma}(\theta) = -N_{\alpha}(\theta) \end{cases}$$
 (21)

For the combinations $6s/24p_s/11p_r$ $(13p_r)$, $12s/24p_s/11p_r$ $(13p_r)$, $6s/18p_s/8p_r$ $(10p_r)$, and $6s/12p_s/5p_r$ $(7p_r)$, the winding function can be expressed as

$$\begin{cases} N_{\alpha}(\theta) = \sum_{i=1}^{\infty} N_{\alpha i} \sin j\theta \\ N_{\beta y}(\theta) = -N_{\alpha}(\theta) \end{cases}, j = 2i - 1$$
(22)

The constant term N_{a0} and the Fourier series coefficients N_{ai} are presented in Table 10 and Table 11, respectively.

Table 10. Constant term of the Fourier series of the winding function.

W110110111	
Cases	N_{a0}
$3s/24p_s/11p_r$ ($13p_r$)	$\frac{4N_{sc}}{\pi}(\theta_{s2}-\theta_{s1})$
$3s/18p_s/8p_r (10p_r)$	$\frac{3N_{sc}}{\pi}(\theta_{s2}-\theta_{s1})$
$9s/18p_{s}/8p_{r}(10p_{r})$	$\frac{N_{sc}}{\pi}(\theta_{s2}-\theta_{s1})$
$3s/12p_s/5p_r$ (7p _r)	$\frac{2N_{Sc}}{\pi}(\theta_{s2}-\theta_{s1})$

Table 11. Fourier series coefficients of the winding functions.

Cases	N _{αi}
$3s/24p_s/11p_r(13p_r)$	$\frac{2N_{sc}}{\pi i}(\sin i\theta_{s2} - \sin i\theta_{s1} + \sin i\theta_{s4} - \sin i\theta_{s3} + \sin i\theta_{s6} - \sin i\theta_{s5} + \sin i\theta_{s8} - \sin i\theta_{s7})$
6s/24p _s /11p _r (13p _r) 12s/24p _s /11p _r (13p _r)	$-\frac{4N_{sc}}{\pi j}(\cos j\theta_{s10} - \cos j\theta_{s9} + \cos j\theta_{s12} - \cos j\theta_{s11})$
$3s/18p_s/8p_r$ ($10p_r$)	$\frac{2N_{sc}}{\pi i}(\sin i\theta_{s2} - \sin i\theta_{s1} + \sin i\theta_{s4} - \sin i\theta_{s3} + \sin i\theta_{s6} - \sin i\theta_{s5})$
$6s/18p_s/8p_r$ ($10p_r$)	$-\frac{4N_{sc}}{\pi j}(-\cos j\theta_{s7}+\cos j\theta_{s8}-\cos j\theta_{s9})$
9s/18p _s /8p _r (10p _r)	$\frac{2N_{sc}}{\pi i} \left[\sin i\theta_{s2} - \sin i\theta_{s1} + \sin i\theta_{s4} - \sin i\theta_{s3} + \sin(i\pi - i\theta_{s2}) - \sin(i\pi - i\theta_{s1}) \right]$
$3s/12p_s/5p_r$ (7p _r)	$\frac{2N_{sc}}{\pi i}(\sin i\theta_{s2} - \sin i\theta_{s1} + \sin i\theta_{s4} - \sin i\theta_{s3})$
$6s/12p_s/5p_r$ (7p _r)	$-\frac{4N_{sc}}{\pi j}(\cos j\theta_{s6}-\cos j\theta_{s5})$

The PM flux linkages of the MTFSPM machine in module α and module $\beta(\gamma)$ can be expressed as

$$\begin{cases} \psi_{\alpha}(t) = k_{w} r_{g} L_{a} \int_{0}^{2\pi} B_{PM\alpha}(\theta, t) N_{\alpha} d\theta \\ \psi_{\beta \gamma}(t) = k_{w} r_{g} \frac{L_{a}}{2} \int_{0}^{2\pi} B_{PM\beta \gamma}(\theta, t) N_{\beta \gamma} d\theta \end{cases}$$
(23)

where k_w represents the winding factor, r_g is the radius of the air-gap, and L_a is the axial length of module α . For the combinations $3s/24p_s/11p_r$ ($13p_r$), $3s/18p_s/8p_r$ ($10p_r$), $9s/18p_s/8p_r$ ($10p_r$), and $3s/12p_s/5p_r$ ($7p_r$), when $|q\pm kp_r|=i$, (20) is non-zero. For the combinations $6s/24p_s/11p_r$ ($13p_r$), $12s/24p_s/11p_r$ ($13p_r$), $6s/18p_s/8p_r$ ($10p_r$), and $6s/12p_s/5p_r$ ($7p_r$), when $|q\pm kp_r|=j$, (20) is non-zero.

Based on Faraday's law, the back-EMF of the MTFSPM machine can be expressed as

$$\begin{cases} e_{\alpha}(t) = -\frac{d\psi_{\alpha}(t)}{dt} \\ e_{\beta}(t) = -\frac{d\psi_{\beta}(t)}{dt} \end{cases}$$
 (24)

Substituting (19), (20), (21), and (23) into (24), the back-EMF for the combinations $3s/24p_s/11p_r$ (13 p_r), $3s/18p_s/8p_r$ (10 p_r), $9s/18p_s/8p_r$ (10 p_r), and $3s/12p_s/5p_r$ (7 p_r)

can be obtained as

$$e_{\alpha}(t) = -\frac{\pi}{2} k_{w} r_{g} L_{a} k P_{r} \omega_{r} \sum_{n=1}^{\infty} \sum_{k=1}^{\infty} F_{PMn} \Lambda_{Rb} \Lambda_{Rk} N_{\alpha i} \cos[k P_{r}(\omega_{r} t + \theta_{0})]$$
(25)

$$e_{\beta}(t) = \frac{\pi}{2} k_{w} r_{g} L_{a} k P_{r} \omega_{r} \sum_{n=1}^{\infty} \sum_{k=1}^{\infty} F_{PMn} \Lambda_{Rb} \Lambda_{Rk} N_{cai} \cos[k P_{r}(\omega_{r} t + \theta_{0} + \frac{\pi}{P_{r}})]$$
(26)

Substituting (19), (20), (22), and (23) into (24), the back-EMF for the combinations $6s/24p_s/11p_r$ ($13p_r$), $12s/24p_s/11p_r$ ($13p_r$), $6s/18p_s/8p_r$ ($10p_r$), and $6s/12p_s/5p_r$ ($7p_r$) can be obtained as

$$e_{\alpha}(t) = \frac{\pi}{2} \operatorname{sgn}(q \pm kP_r) k_w r_g L_a k P_r \omega_r \sum_{n=1}^{\infty} \sum_{k=1}^{\infty} F_{PMn} \Lambda_{Rb} \Lambda_{Rk} N_{\alpha i}$$

$$\times \sin[kP_r(\omega_r t + \theta_0)] \tag{27}$$

$$e_{\beta}(t) = -\frac{\pi}{2} \operatorname{sgn}(q \pm kP_{r}) k_{w} r_{g} L_{a} k P_{r} \omega_{r} \sum_{n=1}^{\infty} \sum_{k=1}^{\infty} F_{PMn} \Lambda_{Rb} \Lambda_{Rk} N_{\alpha i}$$

$$\times \sin[kP_{r}(\omega_{r} t + \theta_{0} + \frac{\pi}{P_{r}})]$$
(28)

The total back-EMF of the MTFSPM machine can be expressed as

$$e(t) = e_{\alpha}(t) + 2e_{\beta}(t) \tag{29}$$

Based on (25) to (29), the fundamental back-EMF amplitudes for different $N_s/P_s/P_r$ combinations of the MTFSPM machine can be calculated, as shown in Fig. 12. It can be observed that the analytical trends match the FEA results. Through the analysis of the analytical results, the following conclusions can be drawn:

- 1) For P_s =24, 18, and 12, the optimal $N_s/P_s/P_r$ combinations are $6s/24p_s/13p_r$, $6s/18p_s/10p_r$, and $6s/12p_s/7p_r$, respectively.
- 2) For P_s =24, the 6-slot machines exhibit the highest back-EMF amplitudes, which can be attributed to two main factors: First, although the 3-slot machines have fewer slots, the winding factors of the 3-slot machines (0.829) are lower than those of the 6-slot machines (0.958). Second, although the winding factors of the 12-slot machines (0.991) are higher than those of the 6-slot machines (0.958), the 12-slot machines have more slots, which significantly affects the PM-MMF amplitudes. Therefore, both the winding factor and the number of slots should be comprehensively considered to select the machines with optimal $N_s/P_s/P_r$ combinations. Additionally, for P_s =18 and 12, the 6-slot machines also achieve the highest fundamental back-EMF amplitudes, with the

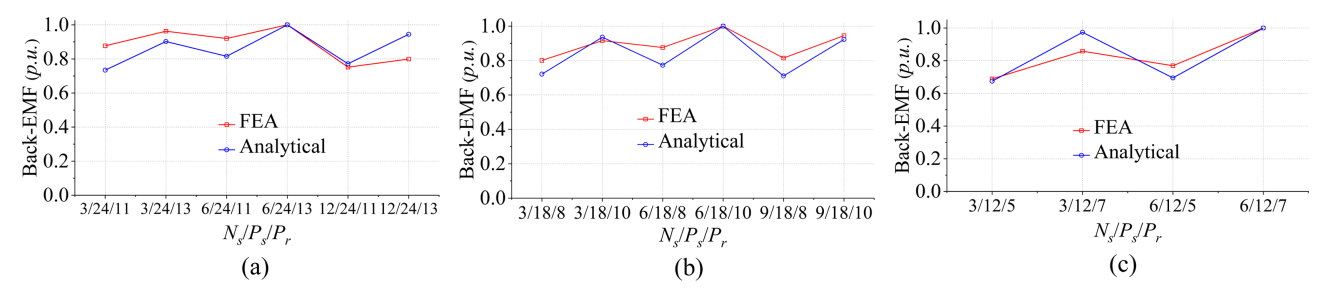


Fig. 12. (Color online) Back-EMF amplitudes. (a) P_s =24. (b) P_s =18. (c) P_s =12.

reasons being similar to those for $P_s = 24$.

3) For the same N_s/P_s , it can be seen that an increase in P_r leads to a higher fundamental back-EMF amplitude. This can be attributed to P_r being a coefficient in the back-EMF equation.

2.3. Phase current analysis

The phase current of the MTFSPM machine can be expressed as

$$I_m = \frac{\sqrt{2}J_s A_{slot} k_{sf}}{N_{ph}} \tag{27}$$

where J_s represents the current density, A_{slot} denotes the slot area, k_{sf} is the slot filling factor, and N_{ph} is the coil turns number.

To ensure fairness in the comparison, when P_s is fixed, the current density, slot area, and slot filling factor are kept consistent across all $N_s/P_s/P_r$ combinations. Therefore, the phase currents I_m for all $N_s/P_s/P_r$ combinations are the same.

2.4. Output torque analysis

From (6), it can be inferred that the output torque is determined by the back-EMF amplitude and the phase current magnitude. As stated in Section II-B, for a given P_s , the phase currents are the same for all $N_s/P_s/P_r$ combinations. Therefore, the output torque is solely determined by the back-EMF amplitude. Fig. 13 shows

the output torques for different $N_s/P_s/P_r$ combinations. It can be observed that the trend of the analytical calculation agrees well with that of the FEA results.

3. Electromagnetic Performance Comparison

To verify the electromagnetic performance of the $N_s/P_s/P_r$ combinations with the highest output torque for a specific P_s , the 6s/24p_s/13p_r, 6s/18p_s/10p_r, and 6s/12p_s/7p_r MTFSPM machines are selected for electromagnetic characteristic analysis. Furthermore, a 6 slot/7 rotor pole (6s/7p) FSPM machine is selected for comparative analysis. To ensure a fair comparison, all four machines have the same outer diameter, effective axial length, and air-gap length, as shown in Table 12. In addition, the rated speed of the three machines is 1500 r/min, and the rated current density is 5 A/mm².

Fig. 14(a) shows the open circuit flux linkage waveforms of the four machines. The flux linkage amplitudes for the $6s/24p_s/13p_r$ MTFSPM, $6s/18p_s/10p_r$ MTFSPM, $6s/12p_s/7p_r$ MTFSPM, and 6s/7p FSPM machines are 2.62mWb, 2.88mWb, 2.68mWb, and 1.71mWb, respectively. As shown in Fig. 14(b), the fundamental back-EMF amplitude of the $6s/24p_s/13p_r$ MTFSPM machine (5.24V) is higher than that of the $6s/18p_s/10p_r$ MTFSPM machine (4.46V), $6s/12p_s/7p_r$ MTFSPM machine (2.89V), and 6s/7p FSPM machine (1.9V).

As shown in Fig. 15(a), the 6s/18p_s/10p_r MTFSPM

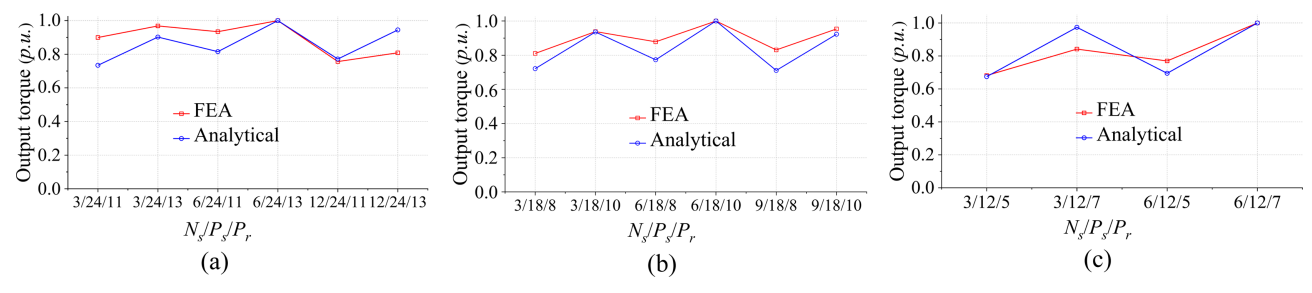


Fig. 13. (Color online) Output torques for different $N_s/P_s/P_r$ combinations. (a) P_s =24. (b) P_s =18. (c) P_s =12.

Items	$6s/24p_s/13p_r$	$6s/18p_s/10p_r$	$6s/12p_s/7p_r$	6s/7p FSPM
Stator outer diameter (mm)	128	128	128	128
Active axial length (mm)	75	75	75	75
Air gap length (mm)	0.35	0.35	0.35	0.35
Rated speed (r/min)	1500	1500	1500	1500
Current density (A/mm ²)	5	5	5	5
Stator tooth width (deg)	10.5	14	21	10
PM width (deg)	4.5	6	9	12.5
Rotor tooth width (deg)	11.43	15.23	18.8	12
Rotor yoke width (deg)	13.85	18.46	27.69	30

Table 12. Parameters of three MTFSPM machines.

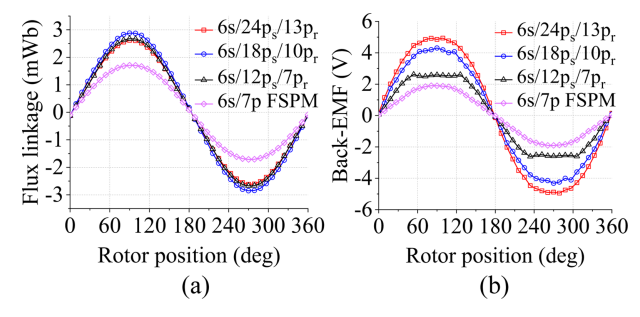


Fig. 14. (Color online) Open circuit flux linkages and back-EMFs of the MTFSPM and FSPM machines. (a) Flux linkages. (b) Back-EMFs.

machine exhibits the highest cogging torque peak-to-peak value (3.66Nm), which is 2.02 times, 2.71 times, and 1.15 times that of the $6s/24p_s/13p_r$ MTFSPM machine, $6s/12p_s/7p_r$ MTFSPM machine, and 6s/7p FSPM machine, respectively. The output torque waveforms of the four machines are shown in Fig. 15(b). The output torque of the $6s/24p_s/13p_r$ MTFSPM machine is 23.98Nm, which is 1.19 times, 1.1 times, and 1.33 times that of the $6s/24p_s/13p_r$ MTFSPM machine, $6s/12p_s/7p_r$ MTFSPM machine, and 6s/7p FSPM machine, respectively. Furthermore, the

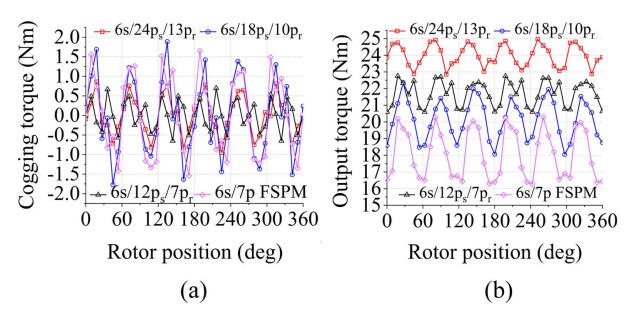


Fig. 15. (Color online) Cogging torques and output torques of MTFSPM and FSPM machines. (a) Cogging torques. (b) Output torques.

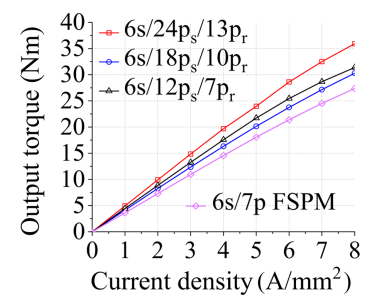


Fig. 16. (Color online) Overload capability of MTFSPM and FSPM machines.

torque ripples of the 6s/24p_s/13p_r, 6s/18p_s/10p_r, and 6s/12p_s/7p_r MTFSPM machines are 8.84%, 21.41%, 9.92%, and 22.22%, respectively. Fig. 16 illustrates the output torques at different current densities for the four machines, indicating that all four machines possess good overload capability. Additionally, at the current density of 5 A/mm², the torque densities of the 6s/24p_s/13p_r, 6s/18p_s/10p_r, and 6s/12p_s/7p_r MTFSPM machines, as well as the 6s/7p FSPM machine, are 24.85Nm/L, 20.86Nm/L, 22.51Nm/L, and 18.72Nm/L, respectively. The corresponding efficiencies of these four motors are 94.8%, 94%, 92.3%, and 93.9%, respectively.

4. Experimental Verification

To validate the torque performance, an optimized 6s/12p_s/7p_r MTFSPM machine was manufactured, as shown in Fig. 17. The experimental platform is shown in Fig. 18. A DC power supply provides the DC bus voltage, while the controller manages the operation of the prototype. The eddy current brake, powered by an independent DC power supply, provides a variable load for the prototype. A torque sensor is installed on the experimental platform to collect torque signals, which are then displayed on the torque display screen.

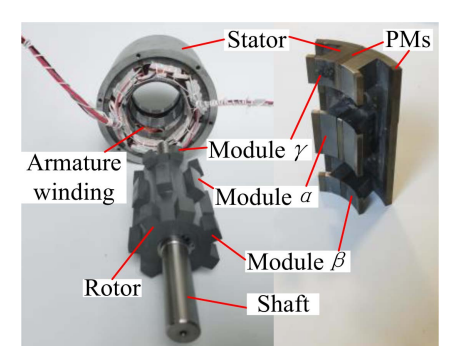


Fig. 17. (Color online) The prototype of the $6s/12p_s/7p_r$ MTF-SPM machine.

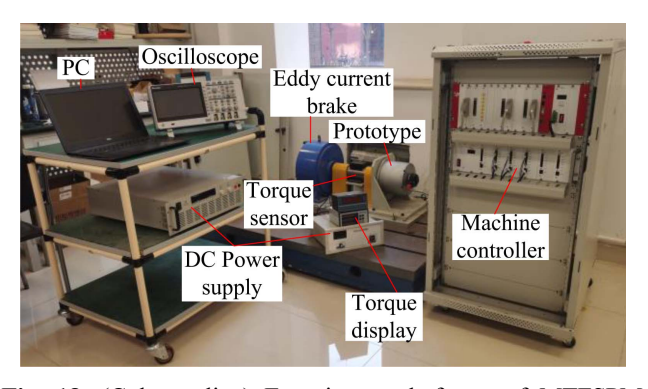


Fig. 18. (Color online) Experiment platforms of MTFSPM machines.

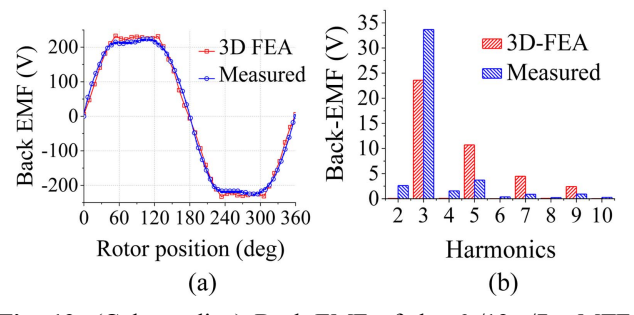


Fig. 19. (Color online) Back-EMF of the 6s/12p_s/7p_r MTF-SPM machine. (a) Flux linkages. (b) Back-EMFs.

The measured and FEA simulated open circuit back-EMF waveforms at 1500r/min are shown in Fig. 19. It can be observed that the measured back-EMF waveform agrees well with the FEA result. According to Fourier analysis, the fundamental amplitude of the measured back-EMF is 251.9V, with only a 1.91% error compared to the 3D-FEA results. The discrepancies between the measured and 3D-FEA results can be attributed to manufacturing tolerances. In addition, the total harmonic distortion (THD) of the measured and 3D-FEA results are 13.56% and 10.43%, respectively. As shown in Fig. 19,

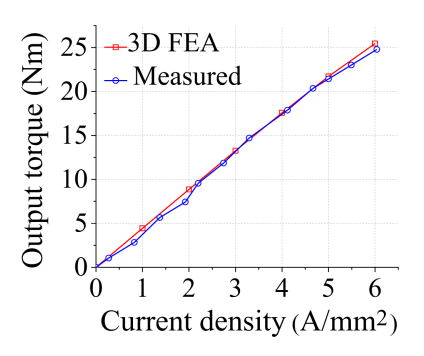


Fig. 20. (Color online) Output torque versus current densities.

both the measured and 3D-FEA results exhibit significant third-order harmonics. The output torque of the MTFSPM machine with current density is shown in Fig. 20. It can be observed that the measured output torque increases approximately linearly with current density, which is in good agreement with the 3D-FEA results.

5. Conclusion

This paper investigates the influence of the $N_s/P_s/P_r$ combinations on the electromagnetic torque performances of the MTFSPM machines, by comprehensively considering the winding factors and the impact of slotting on the amplitude of the PM-MMF. The following conclusions can be drawn:

- 1) By introducing the concept of virtual slots, the distribution factor of the small virtual coils within a practical large coil was calculated. This approach enables the effective determination of the winding factor for MTFSPM machines.
- 2) By employing the magnetic circuit method, the relationship between the PM-MMF amplitudes in the slotted and non-slotted regions can be analyzed. Consequently, the variation of PM-MMF amplitudes for different $N_s/P_s/P_r$ combinations in the MTFSPM machine can be determined.
- 3) The PM-MMF models and the winding function models of the MTFSPM machines for different $N_s/P_s/P_r$ combinations are distinct. By comprehensively considering these models, the variation trends of the back-EMF amplitudes can be obtained, which further leads to the determination of the variation trends of the machine's output torques.
- 4) Under specific values of P_s , both k_w and N_s have an impact on machine's output torque. Therefore, both of these factors should be considered comprehensively during the $N_s/P_s/P_r$ combinations selection. When N_s/P_s are fixed, a higher P_r , as a coefficient of the fundamental

back-EMF, leads to a higher output torque.

Based on the above analysis, the optimal $N_s/P_s/P_r$ combinations for each P_s are obtained, namely $6s/24p_s/13p_r$, $6s/18p_s/10p_r$, and $6s/12p_s/7p_r$ MTFSPM machines. Through 3D-FEA, the electromagnetic performances of these $N_s/P_s/P_r$ combinations and 6s/7p FSPM machine were analyzed. The results indicate that the $6s/24p_s/13p_r$ MTFSPM machine exhibits the highest output torque capability and the lowest torque ripple.

Acknowledgement

This work was supported in part by the Natural Science Foundation of China under Grant 52407072, 52477043 and 52130710; the Natural Science Foundation of Hebei Province under Grant E2024202205 and E2024202298; the Fundamental Research Funds for the Central Universities under Grant 3122025PT20 and Multi-Funding Project of the Tianjin Natural Science Foundation 24JCQNJC00160.

References

- [1] P. Wang, W. Hua, G. Zhang, B. Wang, and M. Cheng, IEEE Trans. Ind. Electron. 69, 2437 (2022).
- [2] F. Zhang, X. Zhu, Z. Xiang, L. Quan, M. Jiang, and S. Zhen, IEEE Trans. Appl. Supercond. **30**, 1 (2020).
- [3] J. Zhu, L. Wu, W. Zheng, Q. Zhou, and T. Li, IEEE Trans. Magn. **57**, 1 (2021).
- [4] X. Li, F. Shen, S. Yu, and Z. Xue, IEEE Trans. Ind. Electron. **68**, 6560 (2021).
- [5] P. Wang, W. Hua, G. Zhang, B. Wang, and M. Cheng, IEEE Trans. Ind. Electron. 69, 12379 (2022).
- [6] T. Liu, P. Su, H. Zhang, T. Yang, and Y. Li, 2023 26th Int. Conf. on Elect. Mach. and Syst. (ICEMS). Zhuhai (2023) pp. 3379-3383.

- [7] E. Afjei, A. Siadatan, and H. Torkaman, IEEE Trans. Magn. 51, 1 (2015).
- [8] D. Bobba, Y. Li, and B. Sarlioglu, 2016 IEEE Transp. Electrific. Conf. and Expo (ITEC). Dearborn (2016) pp. 1-6.
- [9] P. Su, Y. Wang, Y. Li, W. Hua, and Y. Shen, IEEE Trans. Transport. Electrific. **10**, 1947 (2024).
- [10] I. Hasan, T. Husain, Y. Sozer, I. Husain, and E. Muljadi, IEEE Trans. Ind Appl. 55, 3716 (2019).
- [11] A. A. Pourmoosa and M. Mirsalim, IEEE Trans. Ind. Electron. 66, 152 (2019).
- [12] W. Zhang, Y. Xu, and G. Zhou, IEEE Trans. Ind. Electron. **68**, 11223 (2021).
- [13] R. Nasiri-Zarandi, A. Ghaheri, and K. Abbaszadeh, IEEE Trans. Energy Convers. **35**, 445 (2020).
- [14] X. Yang, B. Kou, J. Luo, and H. Zhang, IEEE Trans. Ind. Electron. 68, 4141 (2021).
- [15] X. Zhu and W. Hua, IEEE Trans. Ind. Electron. **66**, 6799 (2019).
- [16] J. T. Chen and Z. Q. Zhu, IEEE Trans. Energy Convers. 25, 293 (2010).
- [17] J. D. McFarland, T. M. Jahns, and A. M. EL-Refaie, IEEE Trans. Ind. Appl. 51, 3041 (2015).
- [18] D. Li, R. Qu, J. Li, W. Xu, and L. Wu, IEEE Trans. Energy Convers. **31**, 106 (2016).
- [19] J. Zhu and L. Wu, IEEE Trans. Ind. Electron. **69**, 2380 (2022).
- [20] C. Wang, Z. Zhang, Y. Liu, W. Geng, and H. Gao, IEEE Trans. Energy Convers. **35**, 1098 (2020).
- [21] P. Kumar and A. M. EL-Refaie, 2022 Int. Conf. on Elect. Mach. and Syst. (ICEMS). Valencia (2022) pp. 1962-1968.
- [22] S. Wang and M. Lin, IEEE Trans. Appl. Supercond. **34**, 1 (2024).
- [23] P. Sun, S. Jia, W. Liu, Z. Yuan, and D. Liang, IEEE Trans. Magn. **60**, 1 (2024).